THE ASTROPHYSICAL JOURNAL, 443:249–260, 1995 April 10

ADAPTIVE OPTICS IMAGING OF PROTO–PLANETARY NEBULAE: FROSTY LEO AND THE RED RECTANGLE

F. RODDIER, C. RODDIER, J. E. GRAVES, AND M. J. NORTHCOTT
Institute for Astronomy, University of Hawaii, Honolulu, Hawaii 96822; roddier, croddier, graves, north@hale.ifa.hawaii.edu
Received 1994 July 28; accepted 1994 October 20

ABSTRACT

Near-infrared, 0".1 resolution images of the bipolar nebulae Frosty Leo and Red Rectangle have been obtained with an adaptive optics system developed at the University of Hawaii. In both cases evidence is found supporting a binary star formation mechanism for the nebulae.

Subject headings: atmospheric effects — infrared: ISM: continuum — methods: observational — planetary nebulae: individual (IRAS 09371+1212, Red Rectangle) — techniques: image processing

1. INTRODUCTION

According to standard models, all stars in the 1–8 $M_\odot$ range become red giants and evolve along the asymptotic giant branch (AGB). During this evolutionary phase the star loses large amounts of mass and surrounds itself with a thick envelope of dust and gas, emitting radiation in the infrared. Pulsations are observed and are generally believed to drive material outside the star to a point where dust condensation occurs. Radiation pressure then drives the dust farther away. A number of objects are now being found that show characteristics of both planetary nebulae and AGB stars. These are called proto–planetary nebulae (PPNs). PPNs are believed to exhibit the early stages of future planetary nebulae when the central source, still at the tip of the AGB branch, is undergoing a left turn in the H-R diagram toward its ending stage as a white dwarf. These objects are interesting to observe since they represent a major stage of stellar evolution. Because their angular dimensions are of the order of the seeing disk, high angular resolution imaging techniques are expected to provide important information on the nature of these objects. According to Bujarrabal, Alcolea, & Planesas (1992), most if not all PPNs show clear signs of a bipolar structure. IRAS 09371+1212, also called the "Frosty Leo" nebula, and the "Red Rectangle" nebulosity associated with HD 44179 are examples of such objects. These are reflection nebulae in which the central source is believed to be obscured inside a thick disk of dust seen almost edge-on, whereas its visible light is scattered toward the observer by the less dense clouds on each side of the disk. We present here high angular resolution images of these two sources.

The mechanism by which these bipolar nebulae are formed is still unknown. Morris (1987) has given strong arguments favoring binary stars as a central source. According to Morris, a second star attracts material ejected by the red giant and forms an accretion disk. This has two effects. First, dust tends to accumulate in the plane of the orbit, effectively obscuring both stars when the orbit is seen edge on. Second, a fast polar wind is created on the second star that blows out dust on each side of the disk. Observational results presented here strongly support Morris's arguments.

2. THE OBJECTS

Attention was first drawn to IRAS 09371+1212 by Forveille et al. (1987) who identified it as an evolved star with substantial CO outflow, and suggested icy grains as the source of its unusual infrared emission. This was confirmed by Hodapp, Sellgren, & Nagata (1988) and Rouan et al. (1988), and the nebula was nicknamed "Frosty Leo." Mauron, Le Borgne, & Picquette (1989) subsequently identified the central star as a K7III or K7II star from the visible light scattered by the nebula and assigned a lower limit of 1 kpc to its distance. CCD imaging (Morris & Reipurth 1990) and polarimetry (Dougados et al. 1990) results strongly suggest a bipolar outflow on each side of a dense disk seen edge-on. Dougados, Rouan, & Lena (1992) measured the grain velocity structure in the ouflow and found an average 9.3 km s^{-1} expansion velocity, significantly lower than the CO expansion velocity of 25 km s^{-1}. The difference was attributed to radiation transfer effects in the envelope. Very recently Beuzit et al. (1994) reported adaptive optics imaging results, and showed indirect evidence for a central binary star.

The Red Rectangle nebula attracted attention as early as 1973 when Cohen et al. (1975) identified the infrared source AFCRL 618−1343 (AFGL 915) with a 9th mag star HD 44179 embedded in a small nebulosity with a marked X shape. On photographs, it gives the object a rectangular aspect. The central star has long been considered as a visual binary (0".14–0".3 roughly north-south separation) with no known orbit. Cohen et al. (1975) have identified its spectrum as that of a B9-A0III star in spite of an excessively large Balmer jump and a considerable infrared excess (Greenstein & Oke 1977). In addition, the star has an unusually low iron abundance (Waelkens et al. 1992). The X shape, best seen in the red, has been interpreted as the projection of a hollow bicone, an interpretation supported by Monte Carlo simulations (Yusef-Zadeh, Morris, & White 1984) and by polarization maps (Perkins et al. 1981). Part of the visible spectrum attributed to the nebulosity is unpolarized and appears as an extended red emission with narrow unidentified features (Schmidt, Cohen, & Margon 1980; Warren-Smith, Scarrott, & Murdin 1981). CH^+ emission lines have been identified in the blue (Balm & Jura 1992). The infrared spectrum is almost featureless between 1.5 and 2.2 μm (Thronson 1982) whereas unidentified emission bands appear at 3.3, 6.2, 7.7, 8.6, and 11.2 μm (Merrill 1977; Russell, Soifer, & Willner 1978). These bands may be related to material seen in absorption in the interstellar medium (Scarrott et al. 1992). Cohen et al. (1986) found they were related to the carbon content of the envelope, favoring their attribution to

polycyclic aromatic hydrocarbons (PAHs), precursors to the formation of carbon grains (Leger & Puget 1984). PAHs, possibly fulleranes, may also explain the anomalies observed by Sitko, Savage, & Meade (1981) in the UV spectrum and the extended red emission (Webster 1993).

High angular resolution speckle techniques have been applied to the Red Rectangle. Using one-dimensional scans, Dyck et al. (1984) observed in *H*, *K*, *L*, and *M* and modeled the source with two components, an extended (0".9) component with wavelength-independent size, identified as scattered light, and a compact component with size increasing at longer wavelength, identified as thermal emission. Dainty et al. (1985) observed in *K*, *L*, and *M*. They found that the extended emission was elongated (1".05 in the north-south direction compared to 0".4 in the east-west direction) and assigned a 0".2 size to the compact emission. Leinert & Haas (1989) observed at *J*, *H*, *K*, *L*, and *M* and produced a tomographic image reconstruction at *K*. They resolved the compact component into a 0".2 source and an unresolved point source offset by 0".15 to the south, which they identified with the star HD 44179. Using two-dimensional data, Christou et al. (1990) produced a *K* image that clearly shows two sources with a 0".15 separation, the fainter source being in the north direction at a position angle of 13°. Observing in the *L* band, Tessier et al. (1990) produced an image showing a strong compact source with wings elongated in the north-south direction and a second much fainter compact source in the east, never seen before.

3. OBSERVATIONS

Observations reported here were made with an experimental adaptive optics system developed by us at the Institute for Astronomy (University of Hawaii). A novel type of wave-front sensor is used to sense wave-front distortions produced by the turbulent atmosphere. This high sensitivity sensor can operate on light sources as faint as 15 mag. Here the observed objects themselves were used to sense the wave front. A deformable mirror called piezo-bimorph is used to partially compensate the wave-front distortions in real time (Roddier, Northcott, & Graves 1991). The system was mounted on an optical bench at the coudé focus of the 3.6 m Canada-France-Hawaii Telescope (CFHT) on Mauna Kea. Only half of the visible light (below 1 μm) was used to sense the wave-front; the other half was used to feed a 1100 × 1100 pixel CCD camera through an interference filter ($\lambda = 8500$ Å, $\Delta\lambda = 75$ Å). Light in the near-infrared (beyond 1 μm) was used to feed the CFHT 256 × 256 pixel NICMOS Camera (Red Eye) through narrow-band filters centered at 1.282 μm ($\Delta\lambda = 0.015$ μm) and 1.647 μm ($\Delta\lambda = 0.018$ μm). Narrow-band filters were used because of chromatic aberrations in the telescope coudé train. The performance of our adaptive optics system has been recently described (Roddier et al. 1994). As for other adaptive optics systems, the point spread function (PSF) consists of a diffraction-limited core surrounded with a halo. The fraction of light in the core varies typically from 40%–50% at 1.65 μm down to 5%–10% at 0.85 μm. Data presented here were recorded during the first successful tests of the instrument. A list of the frames with their characteristics is given in Table 1. For the infrared images, the magnification was 0".025 per pixel which gave a field of view of 6".4 × 6".4. For the CCD camera, it was 0".024 per pixel which gave a field of view of 26".4 × 26".4. Standard data reduction procedures were used for flat-fielding, background subtraction, and data interpolation over bad pixels. Each frame was subsequently rotated to allow for field rotation in the telescope coudé train. The field orientation and pixel size was determined from known binaries α Gem (3".45, 73°.4) and α Psc (1".9, 276°). The values indicated between brackets are the assumed angular separations and position angles for 1993.99. For all the data presented here, north is on top and east on the left. Most of the results presented here are based on features clearly seen on undeconvolved images. However, because adaptive optics provides only a partial compensation, these features often have a low contrast and are difficult to reproduce in prints. For this reason we preferably reproduced deconvolved images. PSFs were recorded on a nearby star between the observations of the science objects and were used to deconvolve the object images. The IRAF Lucy algorithm was used and generally produced good results.

4. THE FROSTY LEO IMAGES

We have selected images obtained under the best seeing conditions and co-added them, taking into account field rotation at the coudé focus. For the Frosty Leo nebula, we averaged six

TABLE 1

LIST OF DATA

Date	Object	Frame Number	Wavelength (μm)	Bandwidth (nm)	Exposure Time (s)
1993 Dec 26.....	Red Rectangle	488	1.647	18	5
		489	...	...	10
		490–493	...	...	60
		290, 292, 293	0.850	75	120
	Frosty Leo	499	...	...	120
		500, 501, 503	...	...	240
		516	1.282	15	60
		517, 518	...	...	600
		522	1.647	18	600
		297–301	0.850	75	120
		310	...	...	240
		311	...	...	360
		312, 316	...	...	600
1993 Dec 27.....	Frosty Leo	820	1.282	15	30
		821, 822	...	...	60
		823	...	...	240
		824–829	1.647	18	240
		328	0.850	75	60
		329–335	...	...	120

120 s exposures taken at 0.85 μm (Nos. 330–335), one 240 s exposure and two 660 s exposures taken at 1.28 μm (Nos. 823, 517, and 518), and three 240 s exposures taken at 1.65 μm (Nos. 825–827). Since the night was not photometric, we arbitrarily normalized to 100 the total flux in each of these average images. Figure 1*a*–1*c* shows contour plots for these average images. The contour levels are indicated for each figure. In all cases, the two lobes of the reflection nebula are clearly seen with a narrow waist corresponding to the presumed almost edge-on disk of dust. In the 1.28 and 1.65 μm images, the central source is seen as a double star with an angular separation of 0.″19. In the 0.85 μm image, the central source only appears as a fuzzy spot close to the northern lobe, and the two components are not resolved. This may be due to the lower efficiency of the adaptive optics system at shorter wavelengths. The east star (on the left) is 68° east from north relative to the west star, that is, the two stars are almost exactly aligned in the plane of the disk. This result in itself gives support to the arguments of Morris (1987). The magnitudes of the two stars are nearly equal both in J and H. A comparison of the peak intensity gives a magnitude difference of 0.02 in J and 0.07 in H, the east star being slightly brighter in both cases. Hence, their spectral type must be similar, K7III according to Mauron et al. (1989). The observed color can be estimated from the photometric results of Rouan et al. (1988). Equating the total flux recorded on our J and H images to, respectively, 8.2 and 7.7 mag, gives for the stars $J-H = 1.45$ mag. This differs from the estimated value $J-H = 0.8$ mag for a K7III star (Bessel &

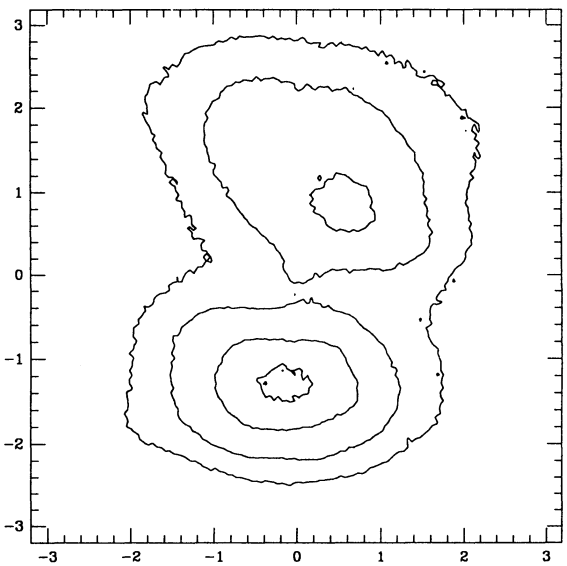

FIG. 1*a*

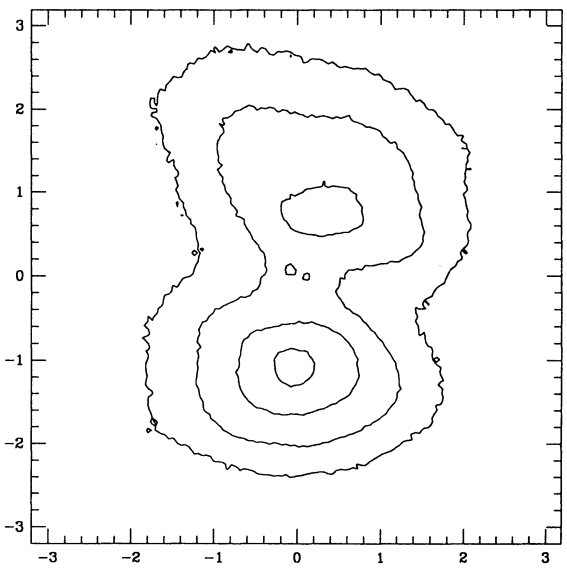

FIG. 1*b*

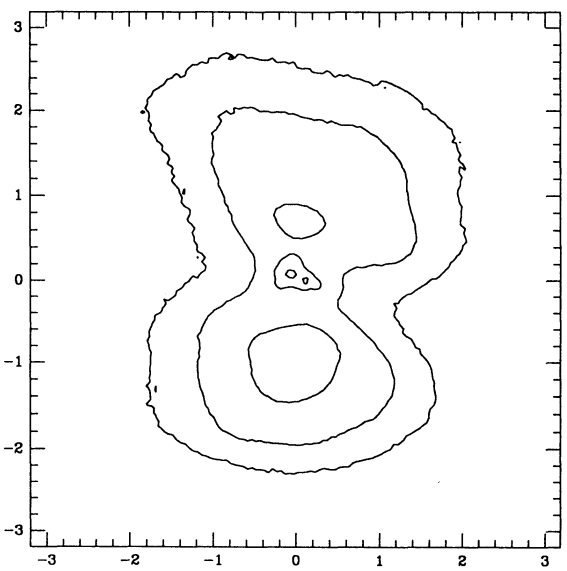

FIG. 1*c*

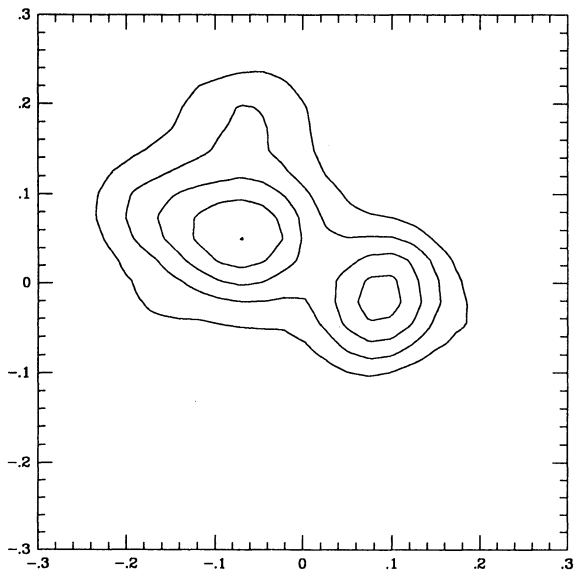

FIG. 1*d*

FIG. 1.—Contour plots of the intensity recorded in the undeconvolved images of Frosty Leo. The total flux in each image has been normalized to 10^6. Intensities are given in flux per 0.″025 pixel. Position coordinates are given in arcseconds. North is up and east is left. (*a*) 0.85 μm image: contour levels are 10, 23, 50, and 75. (*b*) 1.28 μm image: contour levels are 10, 30, 65, and 100. (*c*) 1.65 μm image: contour levels are 10, 30, 80, and 150. (*d*) Enlarged 1.65 μm image: contour levels are 100, 120, 140, 160, 180.

Bret 1988), and gives a color excess of 0.65 mag which can be attributed to the absorption by the dust disk. The ratio of the attenuation factors at J and H is $\exp(-\tau_H)/\exp(-\tau_J) = 1.82$, which gives

$$\tau_J\left(1 - \frac{\tau_H}{\tau_J}\right) = 0.60 . \quad (1)$$

Following Morris & Reipurth (1990), one can assume a λ^{-p} power law for the extinction efficiency with either $p = 1$, or $p = 2$. A value $p = 1$ gives $\tau_H/\tau_J = 0.78$, hence $\tau_H = 2.07$, and $\tau_J = 2.67$. A value $p = 2$ gives $\tau_H/\tau_J = 0.60$, hence $\tau_H = 0.90$ and $\tau_J = 1.50$. These values are higher than those derived by Morris & Reipurth (1990). However, we show below that their result is probably based on a wrong assumption.

If the model of Morris (1987) is correct, one of the two stars (denoted the secondary) is accreting mass from the primary and is the source of a collimated bipolar outflow. The question then arises of which star is the secondary. It seems that an answer can be obtained from the images we have recorded. Figure 1*d* shows enlarged contour levels of the average H image near the two stars. Whereas the west star image (on the right) is round, the east star image is elongated in the direction of the west star. It also has an arm extending toward the north and a hint of another one extending toward the southeast. It must be stated that these are not random speckles. They can be seen on *all* the individual H images. We first thought they were produced by fixed aberrations in the telescope coudé train such as triangular coma, which is not well compensated by our system. However, the fact that they appear around the east star and not the west star rules out this explanation. It is therefore tempting to attribute the elongation of the east star to accreting material and the arms to jets as described by Morris. We used images recorded on a reference star and the IRAF Lucy algorithm to deconvolve out Frosty Leo images. The deconvolved images are shown in Figures 2*a*–2*c* (Plates 2–4). A north-south photometric profile going through the west star is shown in Figure 3. Figure 4 (Plate 6) shows an enlargement of the deconvolved H image. Our experience shows that effects of residual aberrations usually disappear, or are strongly attenuated in the deconvolution process. In this case however, the arms described above are enhanced. They form two jets extending all the way to the lobes of the nebula. There is also a halo of light on the east side of the east star and an elongated prominence on the west side of the west star. These sources are slightly bluer than the stars themselves. We believe that in addition to polar outflows, we also see light scattered by the inner edge of the hollow dust disk. Monte Carlo simulations of light scattered by hollow spheres have indeed indicated that the intensity goes to a sharp maximum at the inner edge (Lefèvre, Bergeat, & Daniel 1982). We note that the two jets are not exactly opposite. Both are inclined by an angle of 20° eastward of the perpendicular to the direction formed by the two stars. We believe that this inclination can be explained by the motion of the secondary star along its orbit.

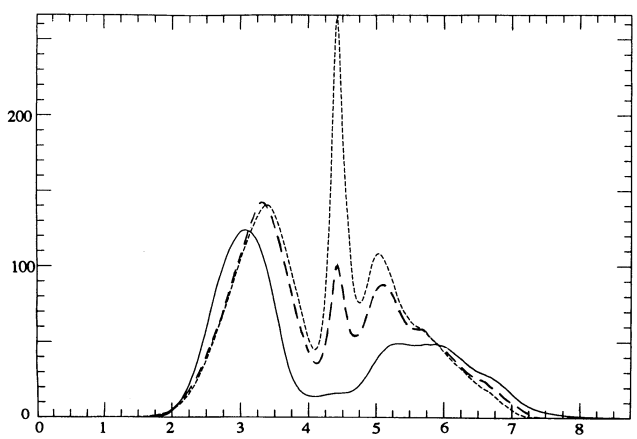

FIG. 3.—Photometric profiles of the Frosty Leo deconvolved images taken along the north-south direction across the west (primary) star. North is on the right side. The horizontal scale is in arcseconds. Intensities have been normalized as in Fig. 1. *Full line*: 0.85 μm image; *long dash*: 1.28 μm image; *short dash*: 1.65 μm image.

To verify this assumption, we have attempted to model the distribution of material ejected by an orbiting star. For simplicity, we assumed that the secondary star was moving along a circular orbit with a constant orbital velocity c_o, and we assumed that material was ejected perpendicular to the plane of the orbit with a constant velocity c_e, the same for both opposite directions. To begin with, we also assumed that the orbit was seen exactly edge-on. We then computed along which lines material ejected in the past would be found today (see Appendix). Two parameters were adjusted, the current position of the secondary star on its orbit and the ratio c_e/c_o. We found that the sharp V shape of the two jets was best reproduced by assuming that the secondary star was near its maximum east elongation, a satisfactory result since the primary star is seen on the west side. The angle of 20° was best fitted with a ratio c_e/c_o between 2 and $\sqrt{2}$ that is an ejection velocity close to or slightly larger than the escape velocity $c_o\sqrt{2}$. The line along which we found material would be distributed has been superposed to Figure 4 in the case where $c_e/c_o = \sqrt{2}$. It matches the observed image quite well. We then attempted to estimate the distribution of material farther away from the nebula and compared the result with the observed aspect of the nebula. Theoretically, the material should be distributed along an helical curve on a nearly conical surface (see Appendix). We found that the distribution of material fitted well the size of the nebula. A ratio c_e/c_o of $\sqrt{2}$ gives a cone semiangle of $\tan^{-1}(c_o/c_e) = 35°$ in agreement with the lateral extent of the lobes. We also found that an even better fit could be obtained by making two minor modifications. First, we dropped the assumption of a constant escape velocity c_e. If material is ejected with a velocity close to the liberation velocity, then owing to gravitational forces, it will slow down as the -0.5 power of the distance (see Appendix). To make the calculations simple we made the approximation that material was still propagating along straight lines but with a velocity decreasing according to the above law. Second, we assumed that the plane of the orbit was slightly inclined from the edge-on position. We found that the best fit was obtained with an inclination angle of the order of 15° to 20°. Figure 2*d* (Plate 5) shows the computed curve superposed to the 0.85 μm image, which best reveals the helical structure. The star is assumed to be at its maximum east elongation and the orbit inclination is 16°, as estimated below from radial velocity measurements. There are of course two mirror symmetric solutions that we cannot distinguish. Morris & Reipurth (1990) and more recently Scarrott & Scarrott (1994) have interpreted the difference in brightness and color between the two lobes of the nebula as evidence for an inclined axis, the north lobe being away from us and seen through the disk. We show below evidence of the

PLATE 2

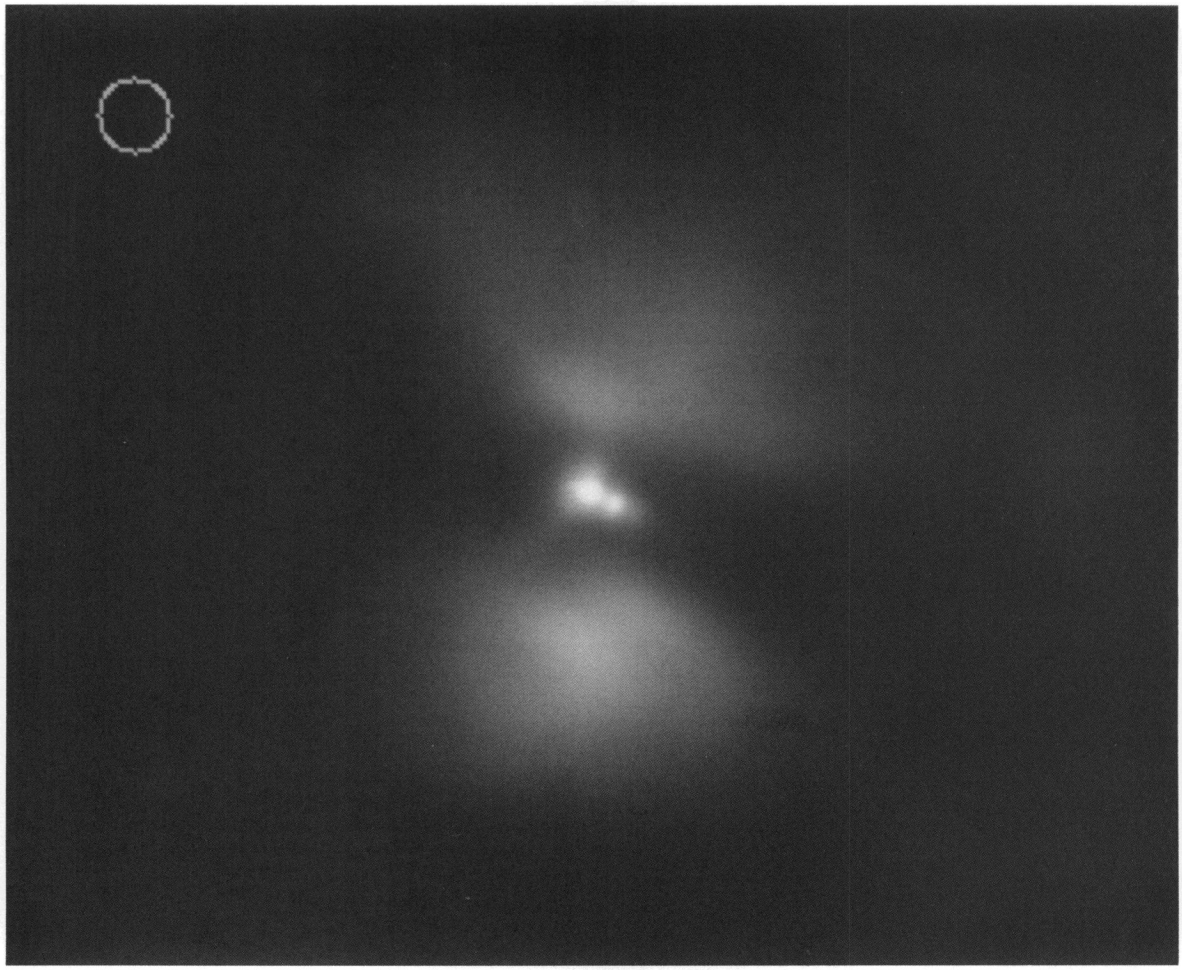

FIG. 2*a*

FIG. 2.—Deconvolved images of Frosty Leo. The scale is given by the 0".5 diameter circle in the upper left corner of the images. North is up, and east is left. Wavelengths are (*a*) 1.65 μm, (*b*) 1.28 μm image, (*c*) 0.85 μm. In (*d*) we have superposed the 0.85 μm image with our estimated theoretical distribution for the material outflowing from an orbiting star. Arrows indicate the directions along which material seems to drift away, presumably under the influence of tidal forces.

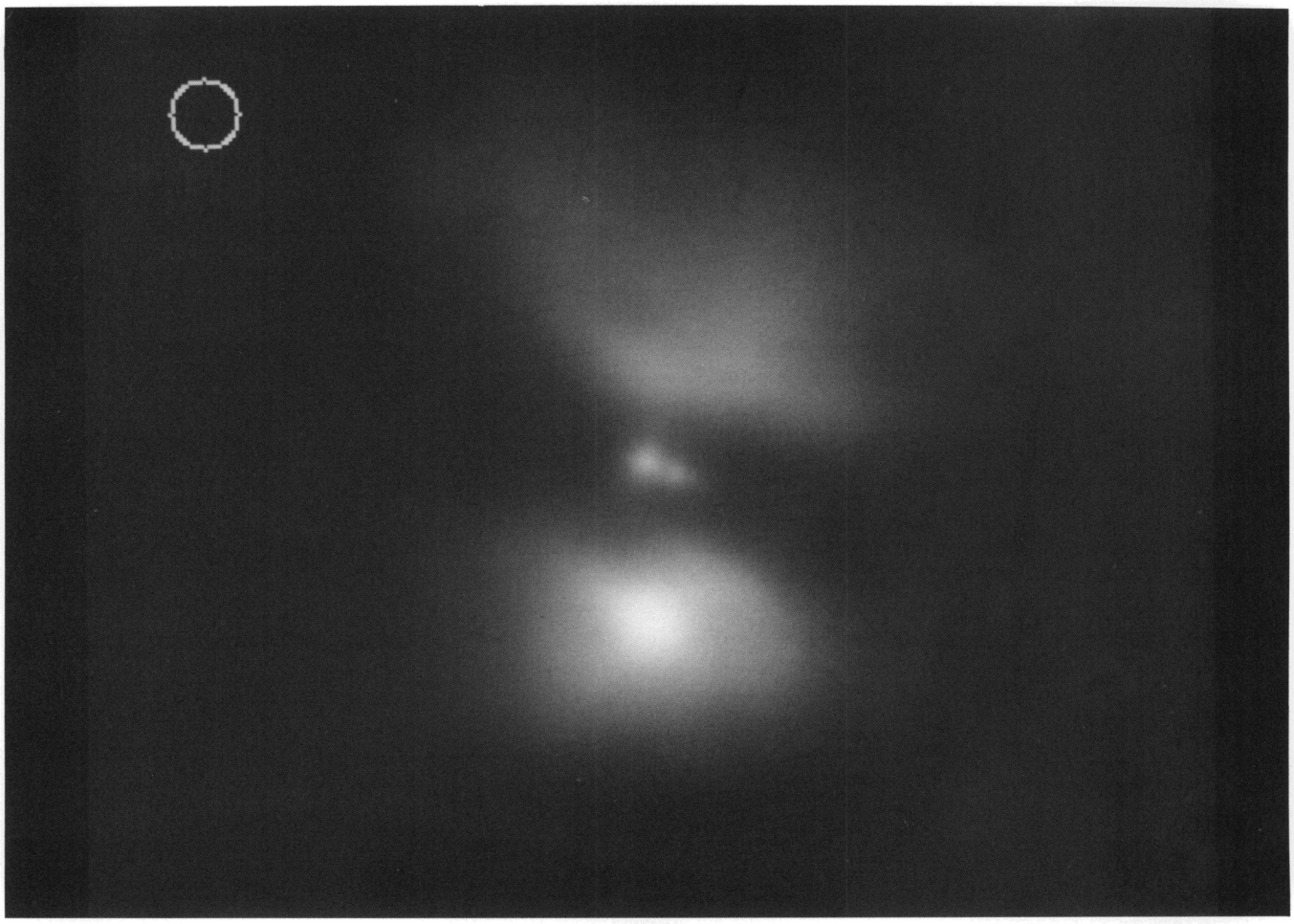

FIG. 2*b*

RODDIER et al. (see 443, 252)

PLATE 4

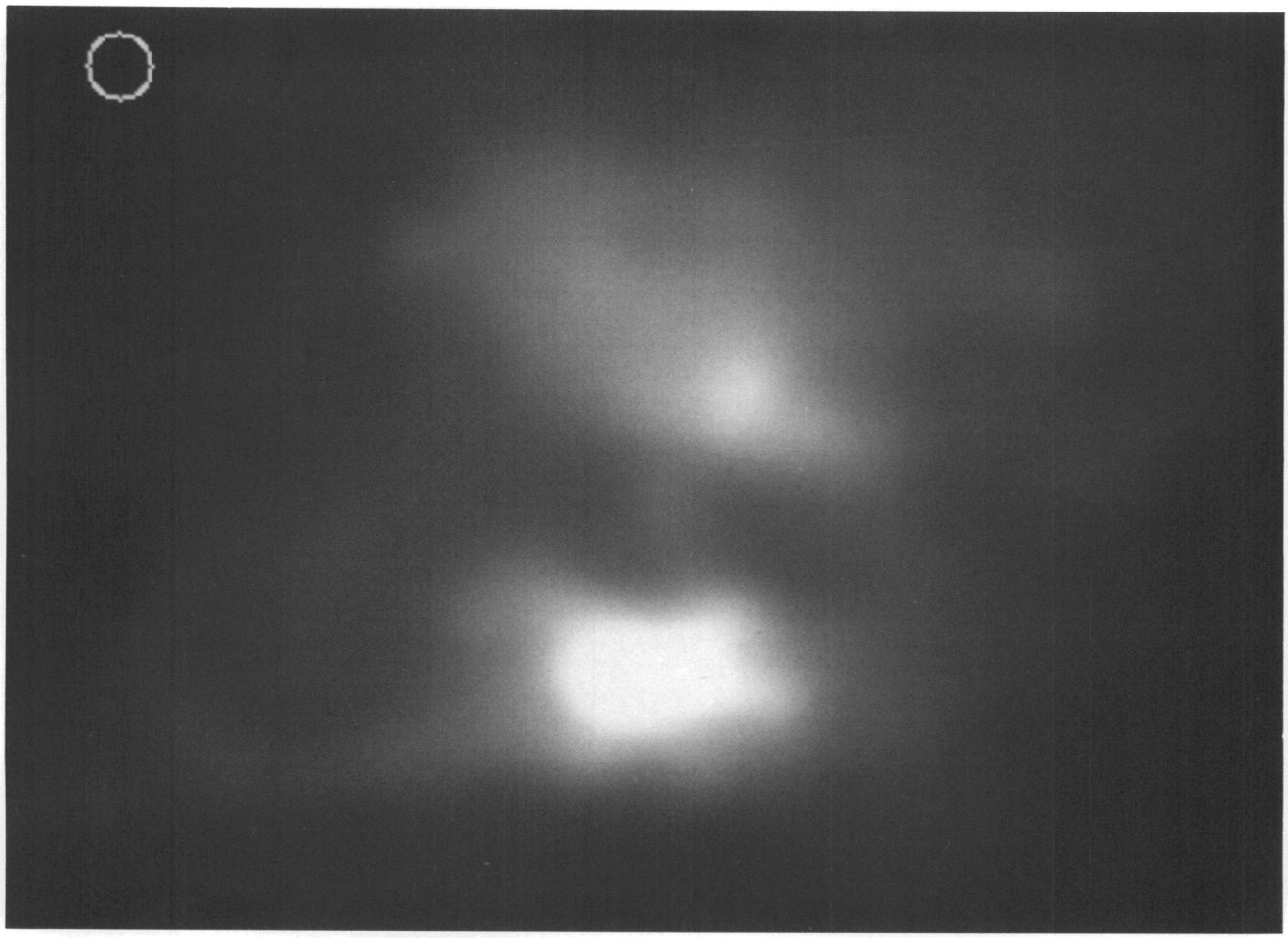

FIG. 2*c*

RODDIER et al. (see 443, 252)

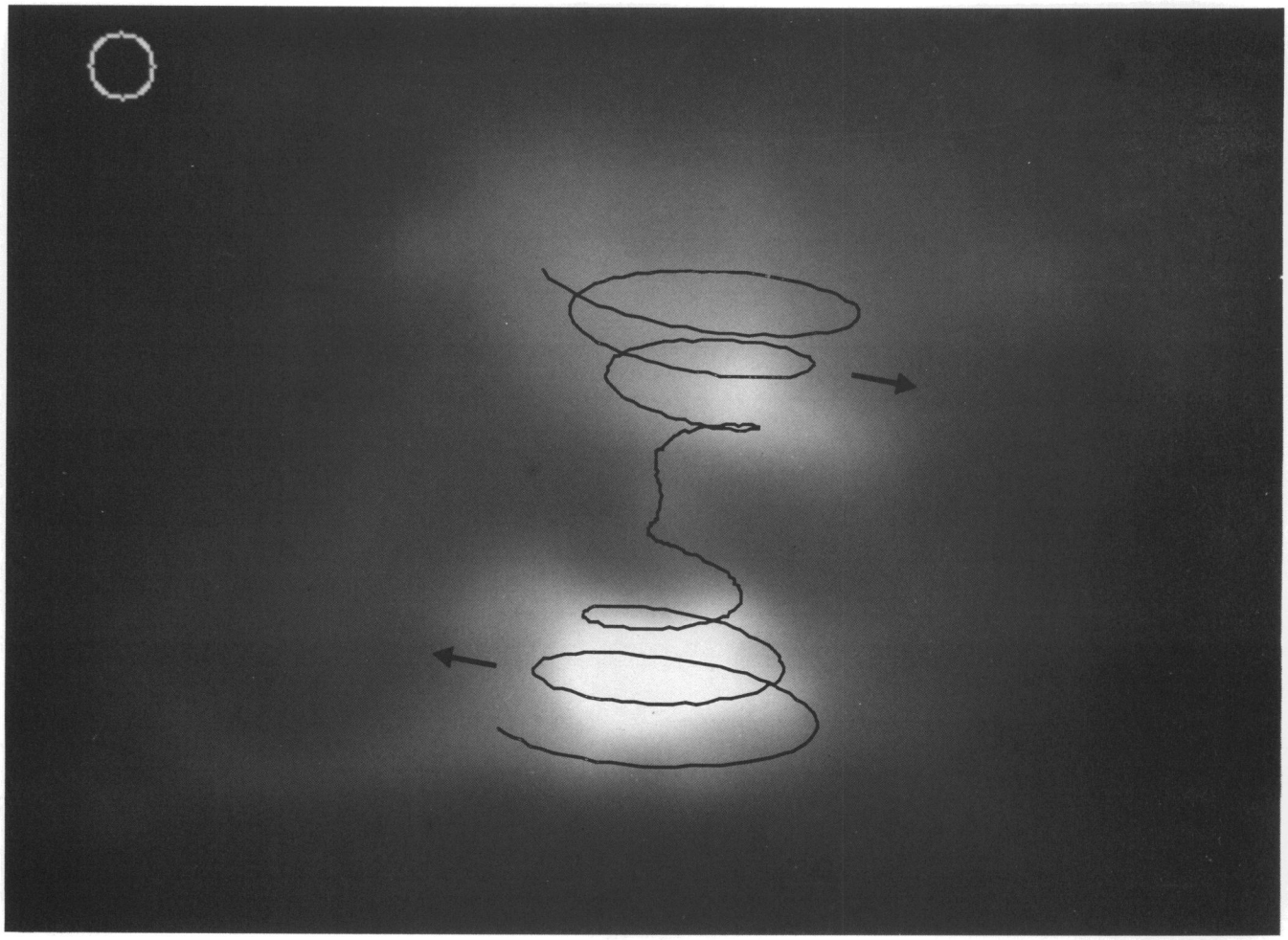

FIG. 2*d*

RODDIER et al. (see 443, 252)

PLATE 6

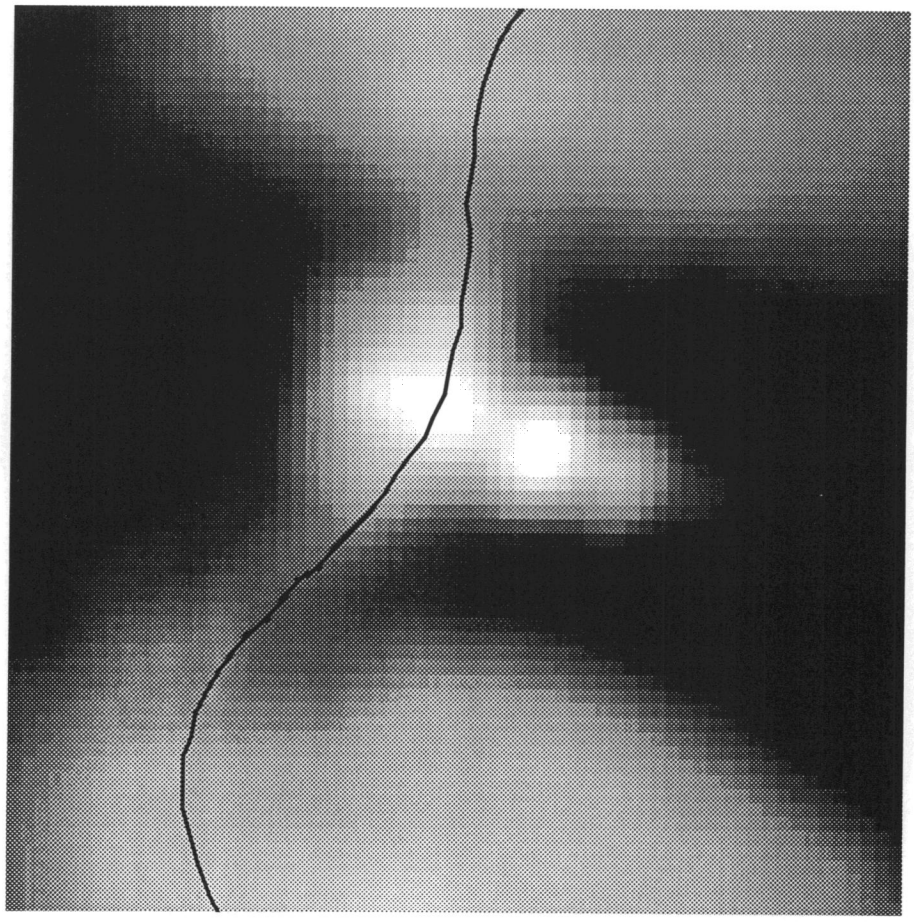

FIG. 4.—Magnified 1".6 × 1".6 area of the deconvolved 1.65 μm Frosty Leo image showing the two stars and the jets outflowing from the east star. North is up and east is left. The superposed curve shows the theoretical distribution of the outflowing material as the star moves along its orbit. The east star is assumed to be at its maximum east elongation, and the ratio of the outflow velocity to the star orbital velocity is $\sqrt{2}$. Both stars are surrounded by a bright halo elongated along the direction of the disk, presumably the bright inner edge of the hollow disk.

RODDIER et al. (see 443, 252)

contrary. If we assume that the north lobe is rather inclined toward us, then the stars are rotating counterclockwise viewed from north.

Evidence that the north lobe is inclined toward us is best seen in the radial velocity distribution measured by Dougados et al. (1992), when interpreted in terms of the above model. The radial velocity was measured as a function of position along the projected axis of the cone. One can distinguish three regions in their plot (Fig. 4 in Dougados et al. 1992). Along the south lobe, the radial velocity is approximately constant and equal to $v_1 = 10$ km s^{-1}. Toward north, the radial velocity drops first down to $v_2 = 4$ km s^{-1}m then climbs up to about $v_3 = 15$ km s^{-1}. We assume that light is scattered by particles moving radially outward along the surface of a bicone. As shown in Figure 5, the radial velocity has two terms: first, a redshift due to the motion of the particle away from the central stars with a velocity we denote c; second, a (generally blue) shift due to the particle velocity projected in the observer direction. We further assume that the bicone is optically thick in the bright region, up to about 3″ from the summit (Fig. 3), and optically thin beyond, where it is much fainter. Then v_1 and v_2 are velocities associated with the *front* surface of the south and north cone. The fact that v_2 is smaller than v_1 indicates a larger blueshift on the north side. Figure 5 shows that the north cone is therefore inclined toward us. The velocity v_3 is measured more than 3″ away from the center. Because the north side is inclined toward us one probably sees here the still optically thick *rear* surface of the north cone through an optically thinner front surface. Additional evidence is given below that the front surface of the north lobe has been pulled apart in this region. If our interpretation is correct, then according to Figure 5,

$$\begin{aligned} v_1 &= c(1 - \cos\theta_1) = c[1 - \sin(\alpha + i)] , \\ v_2 &= c(1 - \cos\theta_2) = c[1 - \sin(\alpha - i)] , \\ v_3 &= c(1 + \cos\theta_2) = c[1 + \sin(\alpha - i)] , \end{aligned} \tag{2}$$

where α is the cone semiangle and i is the inclination of its axis. These equations can be solved for c, α, and i, which gives

$$\begin{aligned} c &= \frac{(v_2 + v_3)}{2} , \\ \alpha &= \frac{1}{2}\left[\sin^{-1}\left(1 - \frac{v_1}{c}\right) + \sin^{-1}\left(1 - \frac{v_2}{c}\right)\right] , \\ i &= \frac{1}{2}\left[\sin^{-1}\left(1 - \frac{v_1}{c}\right) - \sin^{-1}\left(1 - \frac{v_2}{c}\right)\right] . \end{aligned} \tag{3}$$

With the above values for v_1, v_2, and v_3, one gets $c = 12.5$ km s^{-1}, $\alpha = 27°$, and $i = 16°$. The inclination angle is in excellent agreement with the value estimated above (15°–20°). The cone semiangle $\alpha = 27°$ corresponds to an ejection velocity $c_e = c_o/\tan(27°) = 1.96c_o$, that is, a ratio c_e/c_o closer to 2 than to $\sqrt{2}$. There is possibly a large spectrum of velocities in the ejected material.

Further evidence that the north lobe is inclined toward us comes from the apparent location of the stellar sources that are seen closer to the north lobe than to the south lobe. From the data presented in Figure 1, we estimate the ratio d_1/d_2 of the distances from the source to the points of maximum lobe brightness to be 0.67. These two points are in the optically thick region and are therefore associated to the front surface. If we assume that they are symmetric about the sources, then the ratio d_1/d_2 is directly related to the foreshortening angles (Fig. 5*b*) and given by

$$\frac{d_1}{d_2} = \frac{\cos(\alpha + i)}{\cos(\alpha - i)} , \tag{4}$$

which yields

$$\tan(\alpha)\tan(i) = \frac{1 - (d_1/d_2)}{1 + (d_1/d_2)} . \tag{5}$$

Taking $i = 16°$ and $d_1/d_2 = 0.67$ gives $\alpha = 34°$, which is consistent with our other estimates above. Clearly the cone semiangle α is of the order of 30°.

We must now explain why the north lobe is fainter and redder than the south lobe. An obvious explanation is that the south cone is seen almost at normal incidence, whereas the north cone is seen under a more grazing incidence (see Fig. 5). Morris & Reipurth (1990) measured the brightness ratio $R_m(x, \lambda)$ of the two lobes at points oppositely and symmetrically situated about the central stars. They found that the color dependence of this ratio is independent of the radial distance x and conclude that the disk has a constant surface density, an unlikely result. On the contrary, as noted by Scarrott & Scarrott (1994), there must be a strong radial variation in the disk density since only the inner part of the nebula is heavily obscured. We believe that the disk does not extend very far, and obscures neither of the two lobes, except for the inner part less than 1″ from the stars. The measurements of Morris & Reipurth were made in a region where the cone is optically thin. If $\tau(\lambda)$ is the optical thickness perpendicular to the front surface, in the direction of observations it is $\tau(\lambda)\cos\theta_1$ for the north lobe and $\tau(\lambda)\cos\theta_2$ for the south lobe. The brightness ratio then takes the form

$$R_m(x, \lambda) = R_i(x, \lambda)\exp[-\tau(\lambda)(\cos\theta_1 - \cos\theta_2)] , \tag{6}$$

where $R_i(x, \lambda)$ is the ratio of the underlying source brightness. Following Morris & Reipurth (1990), if we assume that $R_i(x, \lambda)$ is wavelength independent, then the color dependence of $R_m(x, \lambda)$ is entirely given by the exponential factor. The fact that it is independent of x comes naturally from the constant angles of the cone surface, and provides further support to our model.

On Figure 2*c* one can see a faint elliptical ring or prominence on the east side of the south lobe (lower left) and apparently a symmetric feature on the west side of the north lobe (upper right). The question arises of why they are found well apart from the main lobes. It seems that the front right part of the north lobe has been ripped off as shown by the arrows in Figure 2*d*, and is drifting away in the west direction. Similarly, the back left part of the south lobe may have also been ripped off, and appears to be drifting away in the east direction. A similar effect can be seen on the image published by Morris & Reipurth (1990) where the nebula appears to be distorted as if the north lobe has been pulled in the west direction, and the south lobe in the east direction. Scarrott & Scarrott (1994) conjecture that this skewness might be produced by the influence of a magnetic field. We rather suggest that this material is drifting away owing to tidal forces exerted by a third star. If our interpretation is correct, then another star must be present either in the northeast or the southwest quadrant. This is indeed the case, as shown by the scan of the Palomar sky survey (POSS) plate published by Forveille et al. (1987). A star of about the same brightness as the nebula can be seen about 1′ away in the northeast direction, at a position angle of 25°. This star has also a faint companion located almost in the direction of the nebula. At the galactic latitude of Frosty Leo (43°) there

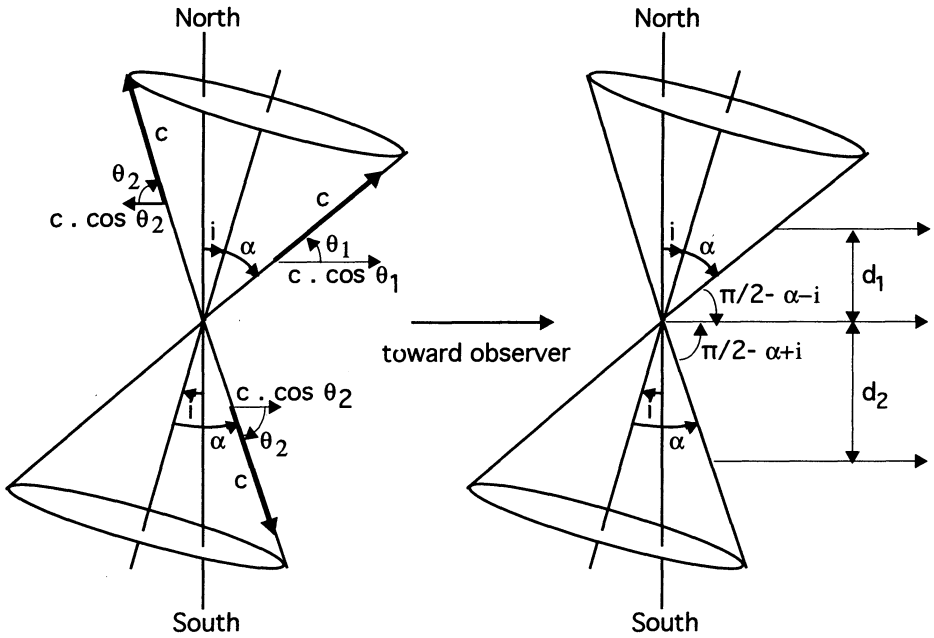

FIG. 5.—Bicone geometry. Outflowing material is assumed to be distributed over the surface of a bicone and to flow radially outward with a velocity c (*left*). Because light from the north lobe is less redshifted than that of the south lobe, the cone must be inclined as shown. Additional evidence comes from the ratio d_1/d_2 of the apparent distance of the source to symmetric points on the lobes (*right*).

are about 15 stars per square degree with $m_V = 11$ or brighter (Allen 1973). Hence the probability of accidentally finding such a star within 1′ of the nebula is only 1.3%. The two objects may therefore be gravitationally linked. Projected on the sky, the extent of the nebula from the core to the ansae is about one-fifth of the distance of the star. If the two objects are linked, then differential orbital motion between the ejected material and the source should produce visible effects. The perturbing star may also cause precession. However, given the distances, the orbital period is at least 5×10^3 times the period of the binary which is the source of the nebula. At the considered timescale, the precession effect would be too small to be noticeable. It should be possible to check this hypothetical gravitational link by measuring the radial velocity of the nearby star with respect to earth. If the two objects are linked then, in the Local Standard of Rest, they should have the same radial velocity of -10 km s^{-1} as measured on the CO line (Forveille et al. 1987). The spectrum of the star could then be used to improve the distance estimate of the nebula. Deeper exposures may also reveal more material scattered away along the same directions.

The radial velocity measurements of Dougados et al. (1992) enabled us to estimate the outflow velocity c at a distance r of approximately 1″ from the stars. The velocity c of the outflowing material is given as a function of r by the relation

$$c^2 - c_\infty^2 = 2\frac{GM}{r}, \tag{7}$$

where G is the gravitational constant, M the attracting mass, and c_∞ the velocity at infinity. In particular, the ejection velocity c_e is given by

$$c_e^2 - c_\infty^2 = 2\frac{GM}{a} = 2c_o^2, \tag{8}$$

where a is the radius of the orbit assumed to be circular, and c_o is the orbital velocity. Subtracting equation (7) from equation (8) gives

$$c_e^2 - c^2 = 2c_o^2\left(1 - \frac{a}{r}\right) \tag{9}$$

or

$$c_o = \frac{c}{\sqrt{(c_e/c_o)^2 - 2[1 - (a/r)]}}. \tag{10}$$

Taking $r = 1''$ and $a = 0''.1$ gives $a/r = 0.1$. With $c = 12.5$ km s^{-1}, and $c_e/c_o = 1.96$, one gets $c_o = 8.75$ km s^{-1}, and $c_e = 17$ km s^{-1}, a value somewhat smaller than the CO expansion velocity estimated to be 25 km s^{-1} by Forveille et al. (1987). It should be noted that material ejected with a higher velocity might be present, but would necessarily be inside the cone, and therefore might be hidden to observations. The "ansae" described by Morris & Reipurth (1990) may have been produced by a high-velocity outburst of material. The masses of rapidly evolving stars are quite uncertain. However, if we assume that both stars are regular K7III stars with 5 $M_\odot$ (Allen 1973), the relation

$$c_o^2 = \frac{GM}{a} \tag{11}$$

gives $a = 127$ AU, and consequently a distance of 1.27 kpc, consistent with the lower limit of 1 kpc given by Mauron et al. (1989). Lower masses yield a smaller orbit and therefore a smaller distance. With the above values, the associated orbital period $T = 2\pi a/c_o$ is 434 yr. The material we see in Figure 2*d* must have been ejected during the last three or four orbits, that is, about $1–2 \times 10^3$ years ago.

5. THE RED RECTANGLE IMAGES

For this object, we averaged all the derotated images taken at 1.65 μm (Nos. 488–493). We also used separately the short

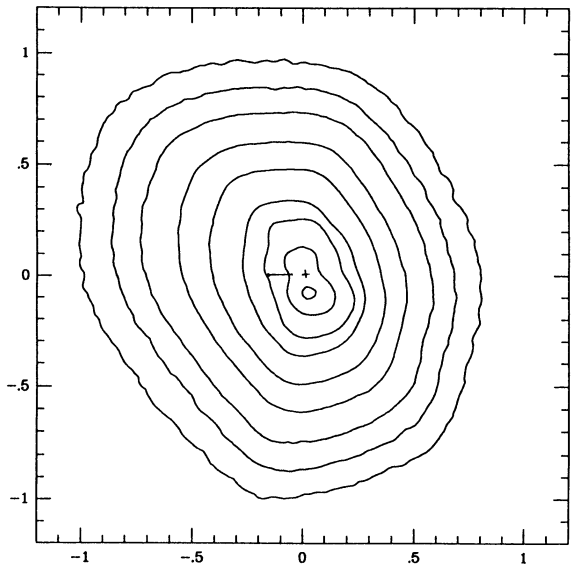

FIG. 6.—Contour plot of the intensity in the undeconvolved 1.65 μm images of the Red Rectangle. North is up, and east is left. The six outer contours are from the average image. The three inner contours are from the highest resolution exposure alone. Position coordinates are given in arcseconds. The center of the coordinates is at the estimated position of the A0 star, as indicated by the cross. The small segment on the left shows the location of the center of gravity of the six outer contours. The total flux has been normalized to 10^6. Intensities are in flux per 0.″025 pixel. Contour levels are 47, 75, 116, 195, 312, 512, 837, 1302, and 1860.

exposure No. 488 which has the highest angular resolution. Figure 6 shows a composite contour plot in which the six large-scale lowest intensity outer contours are from the average image and the three highest intensity inner contours are from the short exposure. At large distances from the center, the nebula appears to be almost circularly symmetric. Figure 7 shows a magnified contour plot of the core in the short exposure. The core is clearly resolved into two sources with an angular separation of 0.″14 and a position angle of 15°. We identify the core with the compact component seen by other observers. We confirm that it is double with a nearly north-south orientation. However, comparison with a reference star shows that both sources are resolved (Figs 8 and 9). Figure 8 shows east-west photometric profiles through the maximum of each lobe in the best undeconvolved image (the two maxima have been normalized to the same value). Figure 8 also shows an east-west profile of a reference star image for comparison. Figure 9 shows photometric profiles of the deconvolved image along the bipolar axis. Profiles of the estimated PSF have been fitted to each maxima. The deconvolved image is shown in Figure 10 (Plate 7). The appearance of the core is that of a very small bipolar nebula with a north lobe and a south lobe. The contour lines of the core shown in Figure 7 are comparable to those of the Frosty Leo nebula (Fig. 1) but for a reduction of the angular size by a factor 13. We estimate that the contribution of the core is only 10% of the total flux, 7.5% for the south lobe, and 2.5% for the north lobe. Unlike the Frosty Leo nebula, *no stellar source* appears in the H band.

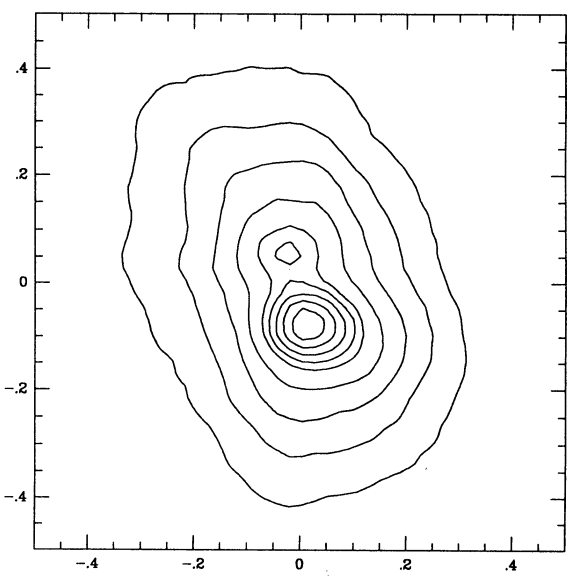

FIG. 7.—Contour plot of the intensity in the core of the Red Rectangle (best undeconvolved 1.65 μm image). North is up, and east is left. Position coordinates are given in arcseconds. The center of the coordinates is at the estimated position of the A0 star. The total flux has been normalized to 10^6. Intensities are in flux per 0.″025 pixel. Contour levels are 465, 698, 930, 1163, 1395, 1535, 1628, 1767, and 1860.

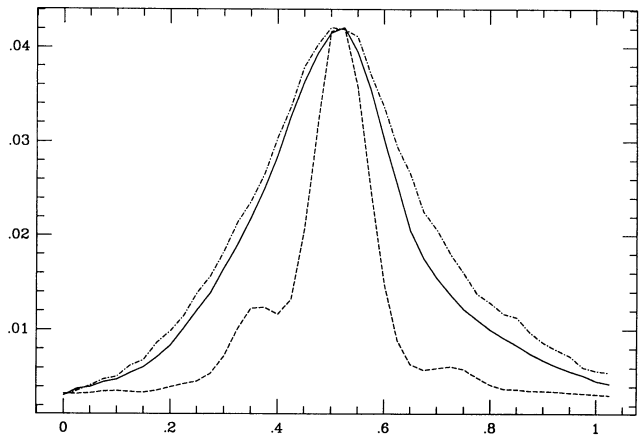

FIG. 8.—Photometric profiles of the undeconvolved images of the two lobes of the Red Rectangle nebula along the east-west direction. East is on the left side. The horizontal scale is in arcseconds. The vertical intensity scale is arbitrary. Profiles have been normalized to the same maximum intensity. *Full line*: South lobe; *dash/dot*: North lobe; *dash*: reference star image.

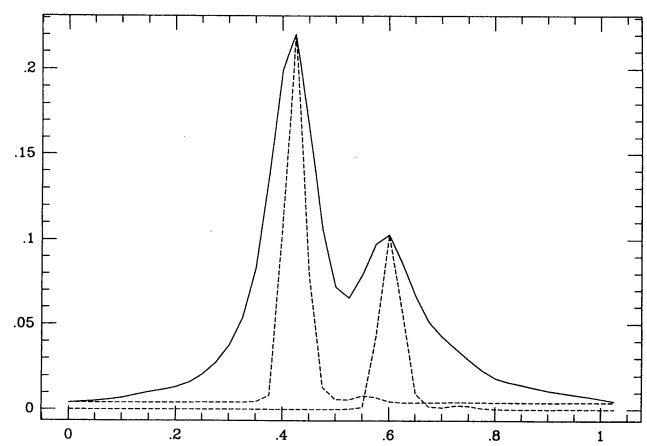

FIG. 9.—Photometric profiles of the deconvolved images of the core of the Red Rectangle nebula along the north-south direction (*full line*). North is on the right side. The horizontal scale is in arcseconds. The vertical intensity scale is arbitrary. Profiles of the estimated point spread function (*dashed line*) centered on the maxima are also shown for comparison.

1995ApJ...443..249R

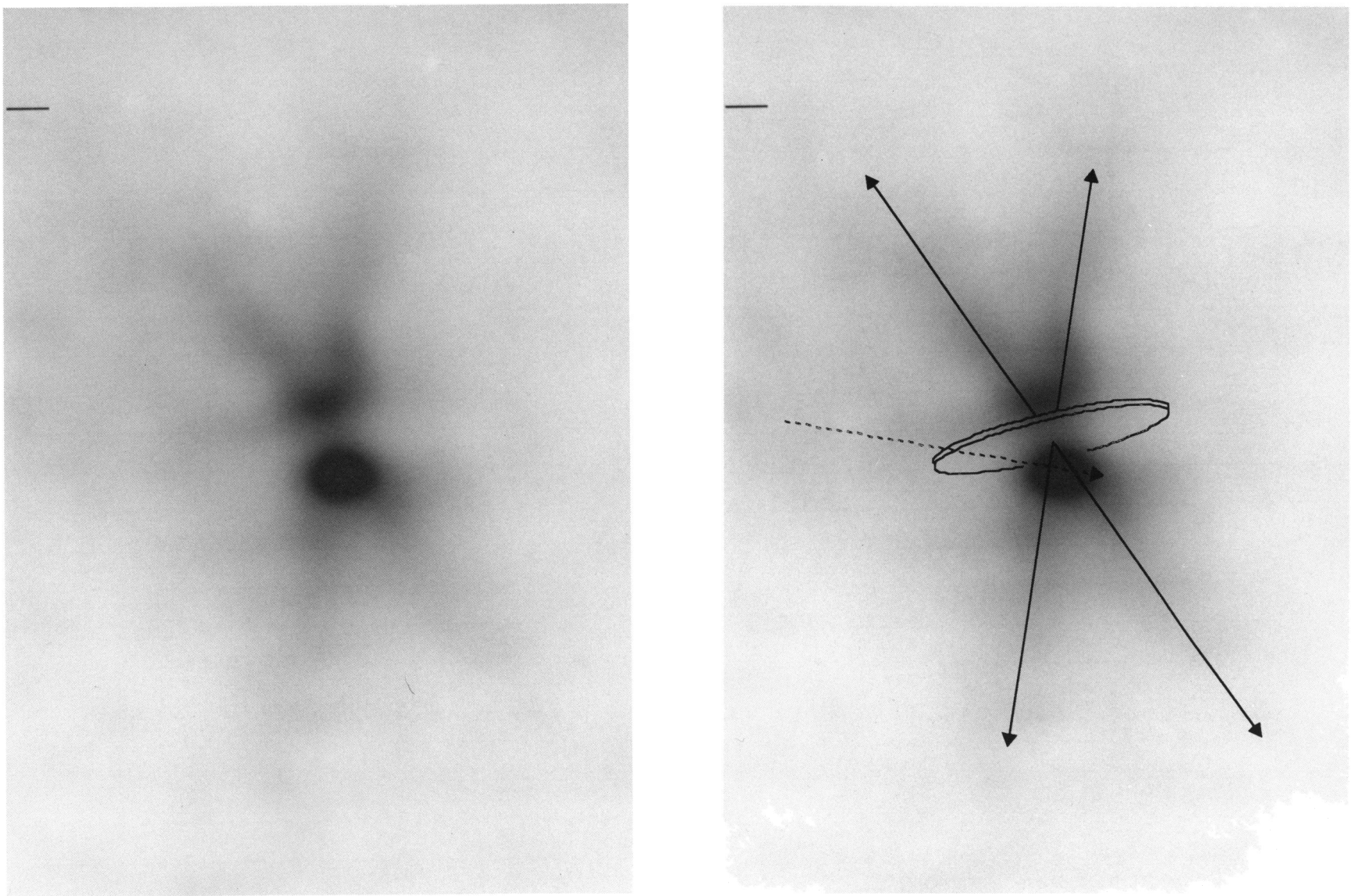

FIG. 10.—Deconvolved image of the Red Rectangle. The scale is given by the 0".1 segment in the upper left corner. In addition to the two bright lobes, one can see the ejection cones, and perhaps an accretion disk as outlined on the right side. The estimated path of the M star is shown with an arrow pointing at its current position. North is up, and east is left.

Images recorded at 0.85 μm essentially show a very similar aspect, but with a lower resolution due to poorer compensation performance. Leinert & Haas (1989) also found a similar aspect in the visible. It is therefore tempting to identify the two lobes with the "binary star" seen by visual observers. The most recent observation is by Heintz (1990). He finds a separation of 0".17 and a position angle of 11°, indeed remarkably close to the above values. The low polarization (less than 1%) observed by Cohen et al. (1975) has often been considered to favor the binary star interpretation. However, these polarization measurements were made with a large aperture (10") which included all the light from the nearly circular symmetric and therefore globally unpolarized extended component. Polarization measurements made with a higher resolution have shown that the nebula is indeed polarized, up to 20% in the blue, whereas in the red 75% of the intensity has been attributed to an unpolarized fluorescence (Perkins et al. 1981). Multiple scattering may also explain these already low values. No polarization measurements have been made with a sufficient angular resolution to isolate the compact core. Since its contribution is only 10% of the total intensity, assuming it has a 5% polarization—as observed in the red for the extended component—gives 0.5% polarization, a result consistent with that of Cohen et al. (1975). In the following we assume that the two sources seen by visual observers are indeed the two lobes of the bipolar nebula. Visual observations will be further discussed below.

Figure 10 is a Lucy deconvolution of the best image. The X shape already seen on our raw images is now clearly visible. It is reminiscent of a similar X shape seen at much longer distances (see photographic plate in Cohen et al. 1975), but it is detected here for the first time very close to the core. The X shape seen at large distances has been interpreted as light scattered by material distributed on the surface of a bicone. We assume that the much smaller X shape seen has a similar origin. The total angle of the small cone is about 40° which is half of the angle of the large cone. The axis of the small cone is oriented at 14° east of north, slightly more than the value of 7° observed for the large cone. As for the large cone, the small cone can be naturally interpreted as evidence for a polar outflow. On the right-hand side of Figure 10, we have outlined the X shape with two straight lines. The two lines clearly intersect between the two lobes pointing at the source of the outflow. We must therefore conclude that the star that produces the outflow is hidden inside a thick disk of dust. Dust is probably pushed away by the outflow so that light from the star leaks on both sides, illuminating the nebula. The spectrum of the scattered light led Cohen et al. (1975) to identify the star with an A0 III star. Figure 10 also shows some evidence for a slightly inclined opaque disk as outlined on the right side. The inclination angle is of the order of 10°, the south side being turned toward us. We identify this disk with the accretion disk described by Morris (1987). If his model is correct, the A star that produces the polar outflow is the secondary star. There must be also a primary star hidden somewhere in the dust. Beuzit et al. (1994) found indirect evidence for a companion star in Frosty Leo by tracking the center of gravity of the nebula intensity contours. We applied the same method to the Red Rectangle. Visual inspection of the contour lines in Figure 6 clearly show that the larger contours are shifted east compared to smaller contours. We found that the center of gravity of the six larger contours were all aligned along the small segment drawn on the east side of the A0 star. It shows evidence that in the past the extended dust cloud was probably formed in this area, and that the source of dust was accelerating toward the west direction. Further evidence is given by the shape of the contour lines in Figure 6 which shows an elongation in the east direction at a position angle of 80° east of north. On the deconvolved image, this elongation appears as a narrow band slightly brighter than the underlying extended nebula. It also appears at longer distances on the 11.3 μm image recently published by Bregman et al. (1993). We are tempted to identify this feature with the excretion disk described by Morris (1987). Note that the excretion disk is almost but not exactly in the same plane as the accretion disk.

Additional evidence for a companion star can be found in the literature. Cohen et al. (1975) have already noted that the infrared radiation of the source cannot be produced by the A star, and hypothesized that a highly luminous companion might be present but hidden in the dust. Greenstein & Oke (1977) also conclude that the nebula radiates more infrared energy than one can get by converting to IR all the energy emitted by the blue star. In this study of radiative transfer in dust clouds, Rowan-Robinson & Harris (1983) estimate that the observed radiation can be produced by an A0 III star plus an M4 III star hidden behind 22 mag of visual extinction. Leinert & Haas (1989) also favor this interpretation. The most direct evidence comes from the reconstructed L-band image published by Tessier et al. (1990) which shows two compact sources aligned in the east-west direction. Indeed, one can expect the stars to become visible through the dust at this wavelength. The hypothetical 22 mag extinction in the visible corresponds to an optical depth of 20. Assuming a λ^{-1} law for the extinction coefficient gives an optical depth of 2.9 at 3.5 μm. A λ^{-2} law gives 0.4. These values are comparable to those given above for the Frosty Leo sources in the J and H bands. We do not know the ratio of the intensities of the two sources observed by Tessier et al. (1990) but if we are dealing with an A0 star and an M4 star, the M4 star will be much brighter in the L band. Hence, from their image, we conclude that the evolved star that is the primary source of the dust is about 0".2 west of the secondary. Again the two stars are aligned with the presumed disk, as we have seen in the Frosty Leo nebula. We believe that the primary star also appears in the data published by Leinert & Haas (1989) but was mistaken for the secondary. Indeed, Tessier's image shows that, apart from the very faint east companion, the L-band aspect of the source is similar to what has been observed at shorter wavelength. If our interpretation is correct, there is, however, a 0".2 westward shift that might have easily eluded the observers in their attempt to register images taken at different wavelengths.

We must now try to understand the time evolution of the object seen by visual observers. Figure 11 shows a polar plot of the position angles and separations observed since 1915. We have plotted all the measurements indicated by Cohen et al. (1975) for which the object was resolved, to which we have added the two recent measurements by Heintz (1990). We have not included the speckle results of Meaburn et al. (1983) which are considered to be erroneous by Heintz (1990). We clearly observe two kinds of behavior. Between 1915 and 1951 the north source was slightly brighter, and a large excursion in position angle occurred between 1941 and 1947. Since 1958, the south source is brighter and little motion is observed. Unless we rule out some of the measurements as uncertain as done by Heintz (1990), it is clearly impossible to understand these changes in terms of an orbital motion of the two sources. However, if we assume that the two sources are the two lobes of a bipolar nebula, then one should expect little or no change

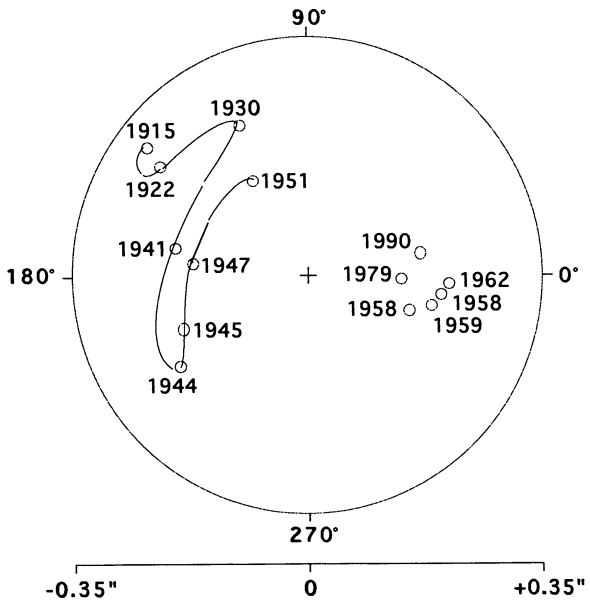

FIG. 11.—Polar plot of the position angle and separation of the two components of the Red Rectangle measured visually since 1915. Large excursions of the position angle were observed around 1940. After that the south component became brighter and the amplitude of the excursions strongly decreased.

at all. Clearly some kind of event occurred around 1944 after which the south lobe became brighter. We have seen evidence that, in the past, the source of the extended dust cloud (a source we identified with the M star) was on the east side of the A star, slightly north of the accretion disk and moving toward the west direction. The M star is now seen on the west side, slightly south of the disk (see drawing in Fig. 10). We may speculate that some of the light from the primary leaks through and contributes to the illumination of the lobes, then its transition from the north side to the south side of the disk explains why the south lobe became brighter after 1951. Moreover, if the primary M star has an eccentric orbit and came in 1944 quite close to the secondary A star, a beam of light from the primary may have shined through the hole in the dust producing a rapid swing of the angle under which the lobes are illuminated.

To scale the whole system, one must estimate values for the distance and the masses of the stars. For the distance, we take the value of 330 pc proposed by Cohen et al. (1975). If we boldly assume that the two stars were very close in 1944, and that the M star has been observed 0".21 away from the A star in October 1989 by Tessier et al. (1990), then the apparent orbital velocity is 70 AU in 45 yr or 7.3 km s^{-1}. For the masses, we will assume again we are dealing with regular A0III and M4III stars with respective luminosities of 106 and 880 solar luminosities (Schmidt-Kaler 1982). Then the masses are given by the mass-luminosity relation (Allen 1973) and are respectively equal to 3.3 and 6.1 $M_\odot$. Assuming a circular orbit, according to equation (11), a total mass of 9.4 $M_\odot$ and a 7.3 km s^{-1} orbital speed give an orbit radius $a = 160$ AU with a 1" angular diameter, and a period of about 600 yr, surprisingly close to the periodicity estimated by Heintz (1990). Smaller masses would give a smaller orbital radius and a smaller period. As described for the Frosty Leo nebula, material ejected by the polar outflows will be helically distributed along the surface of a cone, thus providing a natural explanation for the large cone, extending up to 30" on each side, seen on the photographic plate published by Cohen et al. (1975). There is no need to invoke any precession effect as often done in the literature (Webster 1979; Morris & Reipurth 1990). However, the narrow cone seen in Figure 10 must have a different origin. We have here a close-up view of the polar jets. The conical shape is puzzling. It may be produced by the dust pushed away by expanding gas. Speckle observations recently made by Weghorn (1994) in Hα seem to resolve the north lobe into two sources. Although the observations are interpreted in terms of a triple stellar system, we believe we are seeing here Hα emission sources associated with the polar jets. There may be two jets. A more likely possibility is that the accreting A star is rapidly spinning around an axis different from that of the jet, thus producing a seemingly conical jet.

Some evidence for a large-scale helical distribution of material can be seen in the 11.3 μm image recently published by Bregman et al. (1993) which seems to reveal a periodic structure in the material ejected by the polar outflows. On the other hand, according to our scheme, the 3.3 μm image published by the same authors rather reveals the dust directly surrounding the M star. On Cohen's photograph, the semi-angle of the cone is about 37° which gives a ratio $c_o/c_e = \tan(37°) = 0.75$, close to $1/\sqrt{2}$. However, for the Frosty Leo nebula, we have seen that the cone angle gives a lower limit for the ejection velocity. Hence, the ratio c_o/c_e is probably closer to $\frac{1}{2}$. With the above orbital velocity, a factor $\frac{1}{2}$ would give $c_e = 14.6$ km s^{-1}. We have attempted to estimate the distance between what we believe to be consecutive rings in the Bregman 11.3 μm image. We found an average separation of 3" between rings observed at an average distance of 4" from the center, that is a separation of 990 AU at a distance $r = 1320$ AU. A period of 600 yr gives a velocity $c = 990/600 = 1.65$ AU/yr or 7.85 km s^{-1}. The corresponding ejection velocity c_e is given by equation (9) in § 4. With the above values, one gets $c_e = 19$ km s^{-1}. Ejection velocities probably span at least betwen 14.6 and 19 km s^{-1}, which compares well with the value of 17 km s^{-1} found for the Frosty Leo nebula.

6. DISCUSSION

Let us now compare the two objects. They indeed have similarities. Both are recognized as proto–planetary nebulae with bipolar outflows. For Frosty Leo, we found direct evidence that the source of the outflow is a binary star. For the Red Rectangle, there is compelling indirect evidence that it is also the case. Although the spectral types of the stars are different, their total mass is similar, as well as the orbital speed and ejection velocity. However, the two objects show important differences. In Frosty Leo, the stellar sources are hidden behind a smaller optical depth of dust. The sources already appear in the J band, and most of the dust is concentrated in a large disk, 10^3 AU thick and at least 4×10^3 AU in diameter. On each side of the disk, the brightest points in the lobes are about 2×10^3 AU apart. The lobes themselves extend up to 15×10^3 AU. In the Red Rectangle, the stellar sources are more heavily obscured, and appear only in the L band, perhaps the K band. The dust distribution is mostly spherical, with a diameter of probably a few thousand AU (the small aspherical core contributes to only 10% of the total 1.65 μm flux). There is a hint of a small but probably very dense 15 AU thick and 300 AU diameter disk between the two bright lobes which are only 45 AU apart. Clearly the nature of these lobes is different from

that of the Frosty Leo lobes. We believe that we have here a close up view of two jets, similar to those we barely resolved on each side of the east star in Frosty Leo.

If we follow the model of Morris (1987), it is possible to describe these differences in terms of evolution. Although Frosty Leo is considered to be a very young PPN (Scarrott & Scarrott 1994), under this model the Red Rectangle would be even younger. The evolved, probably pulsating, M star of the Red Rectangle has ejected a large amount of material that has condensed into spherically distributed dust maintained by radiation pressure. This process has been described as the "slow wind" phase of the mass loss. There is only a hint of higher dust concentration along the M star orbit. A thin but very dense accretion disk has formed around the A star on which a lot of hydrogen has already accumulated explaining the unusually large Balmer jump (Greenstein & Oke 1977). Because most of the metals were trapped in dust kept away by radiation pressure, the inflated A star became metal deficient. Since the light reflected by the nebula essentially comes from the A star, this metal deficiency is highly apparent (Waelkens et al. 1992). Owing to a mechanism perhaps similar to those studied for young stars (Pudritz & Norman 1983), the accreting gas has triggered the observed polar outflows, starting what we may identify with the "fast wind" phase described in the literature. Because of the orbital motion of the A star, the outflowing beam describes a cone clearing away the dust from the spherical shell. High-velocity material may be present but would necessarily be inside the cone, and therefore might be hidden. If the outflow is oxygen rich, its oxygen may combine with hydrocarbons in the dust and form CO, which is barely seen in the Red Rectangle but abundant in Frosty Leo, and also H_2O which condenses into the ice crystals of the Frosty Leo nebula. Dust pushed away by the outflow accumulates along the cone surface. Material ejected in the outflow or formed by interaction of the outflow with the dust may also condense along the same surface. Later, owing probably to gravitational forces, dust slowly accumulates in the already denser orbital plane forming a large hollow disk similar to the one observed in the Frosty Leo nebula. Having accumulated a large amount of gas, the A star of the Red Rectangle becomes more massive and its spectral type evolves and gets closer to that of the already evolved star as observed in Frosty Leo. Owing to the loss of angular momentum, the probably elliptical orbit becomes more circular, and its radius may shrink (Livio, Salzman, & Shaviv 1979). However, one difference perhaps subsists between the two objects. The perfect cone of the Red Rectangle may long remain undisturbed, whereas tidal forces have probably long torn apart and made almost unrecognizable the cone of Frosty Leo.

7. CONCLUSIONS

Diffraction-limited images of the Frosty Leo and Red Rectangle nebulae have been obtained in the red and near-infrared. These images demonstrate the performance one can now achieve with adaptive optics. In both cases there is evidence that a binary star is at the origin of these proto–planetary nebulae. The two components of the compact source in the Red Rectangle have been identified with a reflection bipolar nebula produced by polar outflows. Polar ouflows are also seen coming out from one of the two stars at the center of the Frosty Leo nebula. We have shown that material ejected by an orbiting star is helically distributed on a nearly conical surface, which naturally explains the shape of the Red Rectangle nebula. We found that in the Frosty Leo nebula, there is alos evidence for a conical distribution of material, but the cone formation has probably been disrupted by tidal forces. Evidence was given that, contrary to current belief, the north lobe of this nebula is inclined toward us.

These results strongly favor the mechanism proposed by Morris (1987) for the formation of bipolar PPNs. According to Bujarrabal et al. (1992), most, if not all PPNs show clear signs of bipolar structure. From polarization measurements, Johnson & Jones (1991) conclude that aspherical mass loss is likely to be a continual feature of the late stages of stellar evolution. Hence, Morris's mechanism may be the general mechanism by which most of the matter is recycled in the universe. This is a fundamental question that adaptive optics can now help us to answer. If it is the case, the mechanism is a multiple-stage process in which gravitational energy plays a last but perhaps essential role. Not only is a second star necessary to produce the outflow, but also a third star might often further disperse the material away.

Development of the adaptive optics system was supported by NSF grant AST-9020560.

APPENDIX

We derive here the equations we used to trace the distribution of material ejected by an orbiting star. Our coordinate axes are centered at the center of mass of the system with the x-axis oriented toward the observer. The y- and z-axes are in the plane of the sky, with the y-axis in the orbital plane. Let x_0, y_0, and z_0 be the coordinates of the star at the ejection time t_0. Assuming a circular orbit with radius a, we have

$$x_0 = a \cos(i) \cos(\omega t_0),$$
$$y_0 = a \sin(\omega t_0),$$
$$z_0 = -a \sin(i) \cos(\omega t_0), \tag{12}$$

where ω is the star angular velocity, positive if, viewed from above, the star moves counterclockwise. The angle i is the inclination of the orbit, positive if the observer sees the upper side of the orbit. At time t_0, the components of the star velocity are

$$u_0 = -a\omega \cos(i) \sin(\omega t_0),$$
$$v_0 = a\omega \cos(\omega t_0),$$
$$w_0 = a\omega \sin(i) \sin(\omega t_0). \tag{13}$$

The components of the ejection velocity are

$$u_1 = c_1 \sin(i) ,$$
$$v_1 = 0 ,$$
$$w_1 = c_1 \cos(i) , \tag{14}$$

where c_1 is positive for material ejected in the z direction.

As a first approximation, we assume that the ejected particle moves along a straight line with a constant velocity. A particle ejected at time t_0 will be seen at time t_1 at the following position

$$x = a \cos(i) \cos(\omega t_0) + [c_1 \sin(i) - a\omega \cos(i) \sin(\omega t_0)](t_1 - t_0) ,$$
$$y = a \sin(\omega t_0) + a\omega \cos(\omega t_0)(t_1 - t_0) ,$$
$$z = -a \sin(i) \cos(\omega t_0) + [c_1 \cos(i) + a\omega \sin(i) \sin(\omega t_0)](t_1 - t_0) . \tag{15}$$

We now define new variables. Let $\varphi_0 = \omega t_0$ be the orbital phase at the time of ejection, $\varphi_1 = \omega t_1$ the orbital phase at the time of observation, and let $\varphi = \varphi_1 - \varphi_0$ be the phase delay between ejection and observation. Let us also use nondimensional coordinates $X = x/a$, $Y = y/a$, $Z = z/a$, and let $q = c_1/a\omega$ be the ratio of the ejection velocity to the orbital velocity. The coordinates of the particles become a function of φ:

$$X(\varphi) = \cos(i) \cos(\varphi_1 - \varphi) + \varphi[q \sin(i) - \cos(i) \sin(\varphi_1 - \varphi)] ,$$
$$Y(\varphi) = \sin(\varphi_1 - \varphi) + \varphi \cos(\varphi_1 - \varphi) ,$$
$$Z(\varphi) = -\sin(i) \cos(\varphi_1 - \varphi) + \varphi[q \cos(i) + \sin(i) \sin(\varphi_1 - \varphi)] . \tag{16}$$

The apparent distribution of particles on the sky is obtained by plotting the parametric curve $Z(\varphi)$ as a function of $Y(\varphi)$. Apart from the scale given by the orbit radius a, there are three free parameters that can be used to fit the observations, the current phase φ_1 of the star on its orbit, the inclination i of the orbit, and the ratio q of the ejection velocity to the star orbital velocity. The three-dimensional distribution is an helical curve on the surface of an hyperboloid of revolution generated by the straight trajectories that are inclined and rotate along the orbit. A few radii away from the orbit, the hyperboloid is very close to a bicone with its summit at the center of the orbit.

Assuming that particles move along straight lines with a constant velocity is a crude approximation. We will now assume that particles still move along straight lines but with a decreasing velocity due to the gravitational pull of the source. As seen above, the particle speed c is a function of the distance r to the center of mass given by

$$c^2 - c_\infty^2 = 2 \frac{GM}{r} . \tag{17}$$

We will also assume that particles were ejected with just the escape velocity, that is, $c_\infty = 0$. Then, for a straight line motion, the above equation has a simple integral. With $c = dr/dt$, one has

$$\frac{dr}{dt} = \left(\frac{2GM}{r}\right)^{1/2} \quad \text{or} \quad dt = \frac{1}{\sqrt{2GM}} r^{1/2} dr \tag{18}$$

which gives

$$t = \frac{1}{3} \sqrt{\frac{2}{GM}} r^{3/2} \quad \text{and} \quad r = 3^{2/3} \left(\frac{GM}{2}\right)^{1/3} t^{2/3} . \tag{19}$$

With $GM = ac_o^2 = a^3\omega^2$, and $\varphi = \omega t$, the dimensionless distance $\rho = r/a$ has the following expression:

$$\rho(\varphi) = 2^{-1/3}(3\omega t)^{2/3} = 2^{-1/3}(3\varphi)^{2/3} . \tag{20}$$

The direction of motion is the same as before. It is given by a unit vector with components

$$\alpha(\varphi) = \frac{q \sin(i) - \cos(i) \sin(\varphi_1 - \varphi)}{\sqrt{1 + q^2}} ,$$
$$\beta(\varphi) = \frac{\cos(\varphi_1 - \varphi)}{\sqrt{1 + q^2}} ,$$
$$\gamma(\varphi) = \frac{q \cos(i) + \sin(i) \sin(\varphi_1 - \varphi)}{\sqrt{1 + q^2}} . \tag{21}$$

However, since we assumed $c_\infty = 0$, the ratio $q = c_1/a\omega$ must now be taken equal to $\pm\sqrt{2}$. The coordinates of the particles are given by

$$X(\varphi) = \cos(i)\cos(\varphi_1 - \varphi) + \alpha(\varphi)\rho(\varphi),$$
$$Y(\varphi) = \sin(\varphi_1 - \varphi_2) + \beta(\varphi)\rho(\varphi),$$
$$Z(\varphi) = -\sin(i)\cos(\varphi_1 - \varphi) + \gamma(\varphi)\rho(\varphi). \quad (22)$$

In addition to the scale, given by the orbit radius, there are only two free parameters left, the current phase φ_1 of the star on its orbit, and the inclination i of the orbit. The curve plotted in Figure 2*d* was obtained from the above equation with $\varphi_1 = 270°$ and $i = 16°$. The inclination i is found to be positive, which means that if the north lobe is inclined toward us, then viewed from north the star rotates counterclockwise.

Note added in manuscript.—According to E. Tessier (1994, private communication) the faint east source is now thought to be an artifact (improved images reconstructed from the same data as well as from new data do not confirm this result). However, most of the results derived here are still valid if we assume that the M star is now in the line of sight of the south lobe, as the observations made by Leinert & Haas (1989) seem to indicate.

REFERENCES

Allen, C. W. 1973, Astrophysical Quantities (New York: Athlone), 209
Balm, S. P., & Jura, M. 1992, A&A, 261, L25
Bessell, M. S., & Brett, J. M. 1988, PASP, 100, 1134
Beuzit, J.-L., Rouan, D., Thebault, P., & Perrin, G. 1994, A&A, 291, L1
Bregman, J. D., Rank, D., Temi, P., Hudgins, D., & Kay, L. 1993, ApJ, 411, 794
Bujarrabal, V., Alcolea, J., & Planesas, P. 1992, A&A, 257, 701
Christou, J. C., Ridgway, S. T., Buscher, D. F., Haniff, C. A., & McCarthy, D. W., Jr. 1990, in Astrophysics with Infrared Arrays, ed. R. Elston (ASP Conf. Series 14), 133
Cohen, M., et al. 1975, ApJ, 196, 179
Cohen, M., Allamandola, L., Tielens, A. G. G. M., Bregman, J., Simpson, J. P., Witteborn, F. C., Wooden, D., & Rank, D. 1986, ApJ, 302, 737
Dainty, J. C., Pipher, J. L., Lacasse, M. G., & Ridgway, S. T. 1985, ApJ, 293, 530
Dougados, C., Rouan, D., Lacombe, F., Forveille, T., & Tiphene, D. 1990, A&A, 227, 437
Dougados, C., Rouan, D., & Lena, P. 1992, A&A, 253, 464
Dyck, H. M., Zuckerman, B., Leinert, Ch., & Beckwith, S. 1984, ApJ, 287, 801
Forveille, T., Morris, M., Omont, A., & Likkel, L. 1987, A&A, 176, L13
Greenstein, J. L., & Oke, J. B. 1977, PASP, 89, 131
Heintz, W. D. 1990, MNRAS, 245, 759
Hodapp, K.-W., Sellgren, K., & Nagata, T. 1988, ApJ, 326, L61
Johnson, J. J., & Jones, T. J. 1991, AJ, 101, 1735
Lefèvre, J., Bergeat, J., & Daniel, J. Y. 1982, A&A, 114, 341
Leger, A., & Puget, J. L. 1984, A&A, 137, L5
Leinert, Ch., & Haas, M. 1989, A&A, 221, 110
Livio, M., Salzman, J., & Shaviv, G. 1979, MNRAS, 188, 1
Mauron, N., Le Borgne, J. F., & Picquette, M. 1989, A&A, 218, 213
Meaburn, J., Walsh, J. R., Hebden, J. C., Morgan, B. L., & Vine, H. 1983, MNRAS, 205, 53P
Merrill, K. M. 1977, in IAU Colloq. 42, Interaction of Variable Stars with Their Environment, ed. R. Kippenhahn, J. Rahe, & W. Strohmeier, 446
Morris, M. 1987, PASP, 99, 1115
Morris, M., & Reipurth, B. 1990, PASP, 102, 446
Perkins, H. G., Scarrott, S. M., Murdin, P., & Bingham, R. G. 1981, MNRAS, 196, 635
Pudritz, R. E., & Norman, C. A. 1983, ApJ, 274, 677
Roddier, F., Anuskiewicz, J., Graves, J. E., Northcott, M. J., & Roddier, C. 1994, Proc. SPIE, 2201, 2
Roddier, F., Northcott, M., & Graves, J. E. 1991, PASP, 103, 131
Rouan, D., Omont, A., Lacombe, F., & Forveille, T. 1988, A&A, 189, L3
Rowan-Robinson, M., & Harris, S. 1983, MNRAS, 202, 767
Russell, R. W., Soifer, B. T., & Willner, S. P. 1978, ApJ, 220, 568
Scarrott, S. M., & Scarrott, R. M. J. 1994, MNRAS, 268, 615
Scarrott, S. M., Watkin, S., Miles, J. R., & Sarre, P. J. 1992, MNRAS, 255, 11P
Schmidt, G. D., Cohen, M., & Margon, B. 1980, ApJ, 239, L133
Schmidt-Kaler, Th. 1982, in Numerical Data and Functional Relationships in Science and Technology, New Series, Group VI, Vol. 2, Astronomy and Astrophysics, ed. K. Schaifers & H. H. Voigt (New York: Springer), subvolume b, 454
Sitko, M. L., Savage, B. D., & Meade, M. R. 1981, ApJ, 246, 161
Tessier, E., Perrier, C., Lena, P., Michel, G., & Langlet, A. 1990, in Astrophysics with Infrared Arrays, ed. R. Elston (ASP Conf. Series 14), 145
Thronson, H. A., Jr. 1982, AJ, 87, 1207
Waelkens, C., Van Winckel, H., Trams, N. R., & Waters, L. B. F. M. 1992, A&A, 256, L15
Warren-Smith, R. F., Scarrott, S. M., & Murdin, P. 1981, Nature, 292, 317
Webster, A. 1979, MNRAS, 189, 33P
———. 1993, MNRAS, 262, L59
Weghorn, H. 1994, Astr. Gesellschaft Abstract Series, 10, 42
Yusef-Zadeh, F., Morris, M., & White, R. L. 1984, ApJ, 278, 186